1   **A novel positively-charged metal-coordinated nanofiltration membrane for**

2   **lithium recovery**

3   Li Wang[a,b], Danyal Rehman[c], Peng-Fei Sun[d], Akshay Deshmukh[c], Liyuan Zhang[b], Qi

4   Han[a], Zhe Yang[b*], Zhongying Wang[a*], Hee-Deung Park[d], John H. Lienhard[c*] and

5   Chuyang Y. Tang[b]

6   [a] School of Environmental Science and Engineering, Southern University of Science

7   and Technology, Shenzhen 518055, China

8   [b] Department of Civil Engineering, the University of Hong Kong, Pokfulam, Hong

9   Kong, SAR, P. R. China

10   [c] Department of Mechanical Engineering, Massachusetts Institute of Technology,
11   Cambridge MA 02139, USA

12   [d] School of Civil, Environmental and Architectural Engineering, Korea University,

13   Seoul, 02841, South Korea

14

15

16   [*] to whom correspondence should be addressed.

17   Zhongying Wang   e-mail: wangzy6@sustech.edu.cn;   tel.: +86-075588018040;

18   Zhe Yang   e-mail: zheyang@connect.hku.hk;   tel.: +852-2857 8470;

19   John H. Lienhard   e-mail: lienhard@mit.edu.;   tel.: +1-617-253-3790

20

21

Abstract

Nanofiltration (NF) if with high water flux and precise separation performance with high Li^+/Mg^{2+} selectivity, is ideal for lithium brine recovery. However, conventional polyamide-based commercial NF membranes are ineffective in lithium recovery processes due to their undesired Li^+/Mg^{2+} selectivity. In addition, they are constrained by the water permeance-selectivity trade-off, which means that highly permeable membrane often has lower selectivity. In this study, we developed a novel non-polyamide NF membrane based on metal coordinated structure, which exhibits simultaneously improved water permeance and Li^+/Mg^{2+} selectivity. Specifically, the optimized Cu-m-phenylenediamine (MPD) membrane demonstrated a high water permeance of 16.2 ± 2.7 LMH/bar and a high Li^+/Mg^{2+} selectivity of 8.0 ± 1.0, which surpassed the trade-off of permeance-selectivity. Meanwhile, the existence of copper in the Cu-MPD membrane further enhanced antibiofouling property and the metal-coordinated nanofiltration membrane possesses a pH-responsive protperty. Finally, a transport model based on the Nernst-Planck equations has been developed to fit the water flux and rejection of uncharged solutes to the experiments conducted. The model had a deviation below 2% for all experiments performed and suggested an average pore radius of 1.25 nm with a porosity of 0.21 for the Cu-MPD membrane. Overall, our study provides an exciting approach for fabricating non-polyamide high-performance nanofiltration membrane in the context of lithium recovery.

43   **TOC**

Metal-coordinated nanofiltration membrane
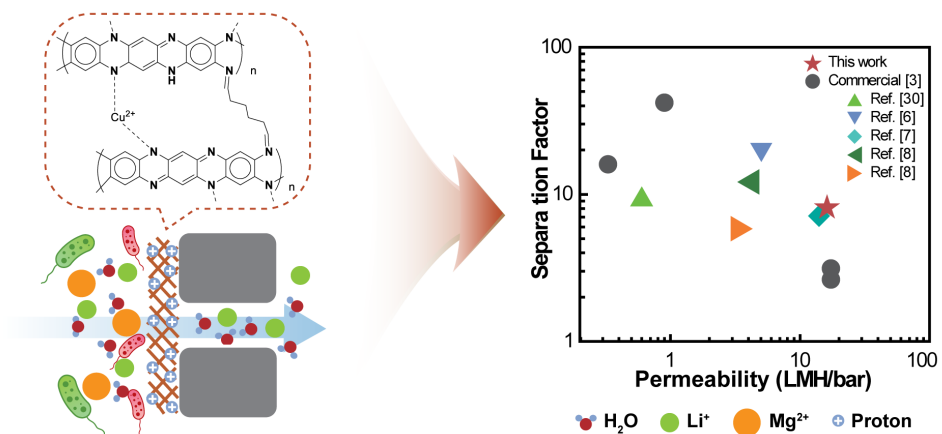
44
45
46

INTRODUCTION

Lithium, the lightest metal, has been extensively applied in rechargeable batteries with numerous important applications such as environmental-friendly vehicles, mobile communication equipment and other electric devices.[1] Lithium can be extracted from aqueous media including salt lakes, brines, and seawater, of which continental brine accounts for approximately ~ 59% of the worldwide lithium production.[2, 3] Therefore, many technologies have been developed to recover lithium from aqueous sources.[4-8] Compared to conventional approaches such as solar evaporation, chemical precipitation, adsorption, and solvent extraction, nanofiltration (NF) offers a promising alternative thanks to its simplicity, low energy consumption, and nontoxicity to the environment.[9-14]

NF is a pressure-driven membrane separation technology,[15] with a molecular weight cut-off (MWCO) ranging from 200 to 1000 Da. Commercial NF membranes adopt a thin-film composite (TFC) structure, where an ultra-thin polyamide rejection layer is formed on the microporous substrate with an interfacial polymerization reaction. The polyamide layer has a charged surface, ensuring an efficient separation of mono- and multi-valent ions at low operating pressures.[11, 16] Nanofiltration in lithium recovery is mainly employed as a pretreatment of the brine to eliminate the unwanted solutes (e.g., magnesium), with the following evaporation process to precipitate and crystallize lithium-related products.[3] Therefore, the high lithium selectivity is preferred to

68   improve the product purity. In addition, high permeance could further translate into

69   enhanced lithium production. Due to the low rejection of lithium ions by the Cu-MPD

70   membrane, there would not be significant lithium dilution to increase the energy

71   consumption in the process of precipitation. Furthermore, a highly-permeable

72   membrane could potentially reduce the energy consumption for the pretreatment by

73   lowering the operation pressure.[17] Consequently, NF has been extensively studied for

74   lithium recovery from brine.[18] Nevertheless, conventional polyamide-based NF

75   membranes are inefficient for achieving more precise membrane selectivity[19, 20] and

76   are adversely constrained by a trade-off between water permeance and selectivity, *i.e.,*

77   higher water permeance resulting in lower selectivity and vice versa.[10, 21-26]

78

79   Given the fact that the permselectivity limits of the polyamide chemistry, exploring

80   non-polyamide materials is critical to overcoming the longstanding tradeoff between

81   water permeance and selectivity.[10, 24, 25, 27, 28] MPD, as one of the crucial monomer (to

82   react with trimesoyl chloride) in fabricating fully-aromatic polyamide RO membrane,

83   has been dominating the RO market since its discovery. Unfortunately, the

84   fully-aromatic RO membrane has relatively low water permeance of 1-3 LMH/bar[10]

85   and RO membranes are also not efficient in Li/Mg selective separation due to the

86   negatively charged membrane surface.[3] For instance, Uyuni salar brine contains 15-18

87   g/L Mg and 0.7-0.9 g/L Li,[29] where Mg can interfere the lithium recovery process by

88   competing with Li in the formation of carbonate precipitate. It is difficult for

89 commercial membrane to selectively remove Mg^{2+} from the brine mixture due to their

90 comparable hydrated radius (Mg of 0.428 nm vs. Li of 0.382 nm).[13] Therefore, we

91 envisage an NF membrane fabricated by the self-polymerization of MPD assisted by

92 Cu^{2+}. Cu^{2+} promots the polymerization and crosslinking and also serves as the

93 positive-charge-center in the NF membrane. Moreover, this fabricating scheme of

94 Cu-MPD membrane can be readily integrated with the existing production line of

95 commercial TFC membrane.

96

97 In this study, we fabricated a non-polyamide NF membrane featuring a

98 positively-charged rejection layer consisting of Cu-MPD complexes. The Cu-MPD

99 complexes imparts the membrane with concurrently high water permeance and

100 enhanced the Mg^{2+}/Li^{+} selectivity. Meanwhile, the pH-responsive nature of the

101 Cu-MPD membrane enables further tuning of water permeance and rejection,

102 showing great potential in lithium recovery application. The fabricated membrane

103 successfully exceeded the state-of-art upper bound pertaining lithium recovery. Our

104 work shall have some insights into future membrane designs in the context of lithium

105 recovery.

106

107 **MATERIALS AND METHODS**

108 **Materials and Chemicals**

109 Deionized (DI) water was produced by Millipore system (Millipore, Billerica, MA)

110 and used for the preparation of all solutions. Polyethersulfone (PES) ultrafiltration

substrate (UH050, MWCO 50 kDa) was purchased from Microdyn Nadir.

m-phenylenediamine (MPD, flakes, 99%, Sigma-Aldrich), $CuCl_2 \cdot 2H_2O$ (Macklin,

China), $NaIO_4$ (99.5%, Macklin, China) and glutaraldehyde (GA, 50% in water,

Aladdin China) were used for fabricating membrane rejection layer. LiCl (anhydrous,

98%) and $MgCl_2 \cdot 6H_2O$ (98%) was purchased from Tokyo Chemical Industry (TCI,

Japan) and Uni-Chem, respectively. D-(+) Glucose (Mw. 180.16, Diekmann), D-(+)

sucrose (Mw. 342.3, Diekmann) and dextran (Mw 1000 and 2000, D-chem) were used

for the evaluation of membrane pore size. Absolute ethanol (≥99.8%) was purchased

from NORMAPUR VWR, Dorset, U.K. All chemicals are analytical grade unless

noted otherwise.

Fabrication of Cu-MPD NF membrane

As shown in Figure 1a, the fabrication protocol of the Cu-MPD NF membrane is

illustrated as follows: a piece of PES substrate (20 × 12 cm) was rinsed with DI water

and mounted into a home-made shaking reactor. First, a certain concentration of MPD

solution was added into the reactor with continuous shaking for 2 min to wet the

substrate surface. Then, $CuCl_2$ solution (1 wt% in DI water) was introduced into the

MPD solution to form the Cu-MPD complexes for 2 min. To accelerate the

polymerization, $NaIO_4$ solution (4 wt% in DI water) was then added into the mixture

and shaken for 5 h at 100 rpm. The membrane was taken out and immersed in DI

water overnight to remove the excessive chemicals. Afterwards, the membrane was

132   crosslinked in GA solution (2 wt% in ethanol solution) at 50 °C for 20 min.[30, 31]

133   Subsequently, the membrane was taken out from the GA ethanol solution and put in

134   an oven of 50 °C for another 20 min for post-treatment.[30] The resultant NF membrane

135   is denoted as CuX-MPD-NF, where X represents the mass ratio of Cu to MPD varied

136   from 0, 1/3, 1/2, 1 and 2.

137

138   **Membrane Characterization**

139   Surface morphologies of the Cu-MPD NF membrane and PES substrate were

140   examined by field emission scanning electron microscopy (FE-SEM, S-4800, Hitachi)

141   at 5 kV. Transmission electron microscopy (TEM, Philips CM100, 100 kV) was

142   utilized to obtain cross-sectional images of the surface layer of the resultant

143   membrane. Prior to characterization, membrane samples were embedded in a resin

144   (Epon, Ted Pella, CA), which was subsequently cut by an Ultracut E ultramicrotome

145   (Reichert, Inc. Depew, NY) into slices with a thickness of around 100 nm. These

146   slices then were placed on a copper grid and characterized in TEM. Atomic force

147   microscopy (AFM, Veeco, Nanoscope IIIa Multimode) was used to evaluate

148   membrane surface morphology and roughness. X-ray photoelectron spectroscopy

149   (XPS, Leybold Sengyang, China) was ultilized to analyze the surface chemical

150   compositions of the membranes. Water Contact angle (Attension Theta, Biolin

151   Scientific Sweden) was employed to measure the water contact angle of the prepared

152   membranes. The streaming potential (SurPASS 3 Electrokinetic Analyzer, Anton

153   PaarGmbH, Austria) was used for testing membrane surface charge. A quartz crystal

154   microbalance with dissipation (QCM-D, E4, QSense Biolin Scientific, Sweden) was

155   applied to examine the structure and mass change of the MPD-Cu complexes.[32]

156   Considering the limitation of QCM-D technique, the step of GA crosslinking was

157   omitted in the preparation of Cu-MPD complexes on the gold sensor. However, the

158   QCM-D measurements adopted the polymerization reaction between Cu^{2+} and MPD,

159   which allows us to reveal the important role of solution pH on affecting the structure

160   and water adsorption properties of Cu-MPD complexes. Therefore, the detailed

161   preparation procedures are described as follows: First, Cu1/2-MPD complex was

162   synthesized by the reaction 40 mL 2% MPD, 40 mL 2% $CuCl_2$ and 20 mL 4% $NaIO_4$,

163   with a polymerization time of 5 hr. The complex solution was further diluted 1000

164   times, and 100 uL of the diluted solution was added onto a gold-coated quartz wafer.

165   Please note that no GA was added for cross-linking due to the limitation of gold

166   sensor. Afterwards, the coated wafer was placed in oven at 60°C overnight for drying.

167   Furthermore, three of the coated wafers were placed in three parallel flow cells in the

168   QCM-D chamber. To initiate the test, pure water was infiltrated into the QCM-D flow

169   cells for 10 min to rinse and stabilize the system and then brines of pH 3, 7, 9 with a

170   concentration of 2000 ppm ($MgCl_2$ and LiCl mixture) were pumped into cells to

171   investigate the pH responsive behavior of the complex (Figure 4a). The frequency and

172   dissipation variation of the three wafers were recorded.

173

174   We further employed QCM-D open cell to investigate of the mechanism of the

175   membrane formation (Figure S6b). First, 200 μL of certain concentration of MPD

176   solution diluted by 10 times was added into the cell and stabilized for a period of time,

177   and then 200 μL of 0.2% $CuCl_2$ was added into it and wait until the frequency of the

178   system stabilized. Finally, 200 μL 0.4% $NaIO_4$ was rapidly added into the cell. The

179   system was further left for reaction until there was no change in the frequency was

180   observed. The frequency was recorded during the whole process and was converted

181   into the thickness of the developed membrane on the surface of the wafer through a

182   Sauerbrey equation.

183

184   The mechanism of QCM-D was described as follows: with a set of QCM-D

185   equipment, one can measure the frequency and dissipation value of the system. The

186   frequency variation can be further converted into mass change or thickness change of

187 the system by a Sauerbrey equation. On the other side, the dissipation value of the

188 coated materials can further translate into the structural change of the membrane.[33]

189

190 **Separation Performance Testing**

191 A cross-flow filtration setup was used to test the separation performance of the

192 membranes. Water permeance and rejection were measured at 5 bar at room

193 temperature, and each membrane was pre-pressured at 6 bar for 2 h to reach the

194 steady-state. Water flux can be calculated according to Eq. (1),

195
$$J_w = \frac{\Delta V}{\Delta t \times A} \tag{1}$$

196 where J_w (L m^{-2} h^{-1}) is the pure water flux; ΔV (L) is the volume of permeate; A (m^2)

197 is the active membrane area and Δt (h) is the sampling time.

198

199 For the rejection measurement, 1000 ppm MgCl$_2$ was used as feed solution. A

200 conductivity meter was used to measure the conductivity of permeate and feed to

201 determine the salt concentrations and then rejection defined by Eq. (2),

202
$$\text{Rej}_i = 1 - \frac{c_p}{c_f} \tag{2}$$

203 where R is the salt rejection, while C_p and C_f are the salt concentrations of the

204 permeate and feed solution, respectively.

205

206 To examine the performance of the membranes in the application of Li recovery from

207 brine, a synthetic brine with a concentration of 2000 ppm (Mg/ Li mass ratio of 23)

208 was used as the feed solution and pH of the feed was adjusted from 3 to 9 using

209   diluted HCl and NaOH solutions.[34] Thus the separation factor $S_{Li,Mg}$ was calculated

210   by Eq. (3),

211                                 $$S_{Li,Mg} = \frac{C_{Li,p}/C_{Mg,p}}{C_{Li,f}/C_{Mg,f}}$$ (3)

212   where $S_{Li,Mg}$ is the separation factor of Li^+ over Mg^{2+}, $C_{Li,p}$ and $C_{Li,f}$ are the Li^+

213   concentration in permeate and feed, respectively, $C_{Mg,p}$ and $C_{Mg,f}$ are the Mg^{2+}

214   concentration in permeate and feed, respectively. Inductive coupled plasma optical

215   emission spectrometer (ICP-OES, Optima 8 × 00, PerkinElmer) was used to measure

216   the concentration of Li^+ and Mg^{2+} according to our previous work.[32]

217

218   **Nanofiltration model for uncharged solutes**

219   The Donnan-Steric Pore model (DSPM) was used to develop a framework to

220   characterize transport across the fabricated Cu-MPD nanofiltration membranes.[35-39]

221   The extended Nernst-Planck equation was applied to model transmembrane transport.

222   For uncharged solutes, the migration term is neglected and transport is governed by

223   convection and diffusion.[40] The resulting expressions are integrated across the

224   membrane yielding closed-form expressions for individual solute fluxes. Water

225   transport is calculated using the Hagen-Poiseuille equation for flow through a tortuous

226   cylindrical pore, in line with observed membrane morphologies. The water and solute

227   fluxes are decoupled and provided by Eq. (4) and Eq. (5), respectively: [37, 39, 41, 42]

228                                 $$J_v = \frac{\epsilon r_p^2 \Delta P}{8\tau\eta L}$$ (4)

229                             $$N_i = \frac{H_{i,C} J_v c_{i,F}}{1 - (1 - H_{i,C}) \exp(-Pe_i)}$$ (5)

230 In Eq. (4), J_v is the volumetric water flux, ϵ is the porosity, r_P is the effective pore

231 radius, τ is the tortuosity, and η is the dynamic viscosity. Across the membrane, ΔP is

232 the applied hydraulic pressure and L is the membrane thickness. A membrane

233 thickness of 0.5 μm was assumed in this work, based on the cross-sectional SEM

234 images of the Cu-MPD membrane active layer (Figure S1). In Eq. (5), N_i is the molar

235 flux of solute i, which is a function of its convective hindrance factor, $H_{i,C}$, Péclet

236 number, Pe_i, and feed concentration, $c_{i,F}$. The permeate concentration of each solute,

237 $c_{i,P}$, is given by molar solute flux divided by the the volumetric solvent flux.

238

239 The Péclet number captures the ratio of convective to diffusive hindrance factors

240 across the membrane and is defined in Eq. (6):

241
$$Pe_i = \frac{K_{i,c} J_v L}{K_{i,d} D_i} \tag{6}$$

242 where, $K_{i,d}$ is the diffusive hindrance coefficient and D_i is the diffusion coefficient of

243 the solute in the solvent. In high Péclet number regimes, convection dominates and

244 the solute flux is primarily governed by the convective hindrance factor, the water

245 flux, and the concentration of the permeate. Conversely, in low Péclet number

246 regimes, the solute rejection is diffusion limited and only depends on the solute flux

247 and permeate concentration.

248

249 Hindrance parameters are usually written as functions of the relative penetrant size,

250 λ_i, where λ_i is defined as the ratio of the solutes' Stokes-Einstein radii to the

251 membrane effective pore radius.[43, 44] In this work, the convective and diffusive

252 hindrance processes are assumed to exhibit activated-type or Arrhenius-like behavior

253 whereby $K_{i,c}$ and $K_{i,d}$ are exponential functions of the convective and diffusive

254 fitting parameters, $\alpha_{i,c}$ and $\alpha_{i,d}$, respectively.[19, 45-48] The mathematical expressions

255 for $K_{i,c}$ and $K_{i,d}$ are given by:

256 $$K_{i,c} = \exp(-\alpha_{i,c}\lambda_i) \tag{7}$$

257 $$K_{i,d} = \exp(-\alpha_{i,d}\lambda_i) \tag{8}$$

258 The semi-empirical parameters $\alpha_{i,c}$ and $\alpha_{i,d}$ in Eq.s (7) and (8) reflect the averaged,

259 temperature-normalized energy barrier associated with solute convection and

260 diffusion processes, respectively. These parameters were used along with the

261 membrane porosity and effective pore radius are determined by the regression of

262 experimental data to the model for uncharged solutes.

263

264 Rejection of each solute species $(1 - c_{i,P}/c_{i,F})$ is given by: [37, 39, 41]

265 $$\text{Rej}_i = 1 - \frac{H_{i,C}}{1-(1-H_{i,C})\exp(-\text{Pe}_i)} \tag{9}$$

266 where Rej_i is the rejection of solute species i. In addition to fitting the rejection of

267 each solute, the model was also fit to the water flux measurements conducted as

268 detailed in Section 2.4. A particle swarm algorithm implemented in Matlab

269 (Mathworks, Natick, MA) was used to minimize the normalized least squared residual

270 between the model and experiments for all uncharged solutes: glucose, sucrose,

271 dextran (1 kDa), and dextran (2 kDa). [37, 39, 41] The objective function and fitted design

272   variables are provided in Eq. (10).

273    $$\text{Obj} = \min_{\epsilon, r_P, \alpha_{i,c}, \alpha_{i,d}} \left\{ \sum_{k=1}^{n_f} \left(\frac{J_{v,k}^{\text{mod}} - J_{v,k}^{\text{exp}}}{J_{v,k}^{\text{exp}}} \right)^2 + \sum_{i=1}^{n_s} \left[\sum_{k=1}^{n_f} \left(\frac{\text{Rej}_{i,k}^{\text{mod}} - \text{Rej}_{i,k}^{\text{exp}}}{\text{Rej}_{i,k}^{\text{exp}}} \right)^2 \right] \right\} \quad (10)$$

274   where the superscripts mod and exp denote the model and experiments. n corresponds

275   to the number of data points collected, where the subscripts s and f denote the

276   experimental data points representing solute rejection and water flux, respectively.

277

278   **Anti-biofouling test**

279   *Pseudomonas aeruginosa* PA14 was used as the model gram-negative bacteria for all

280   anti-biofilm and anti-biofouling assays. Approximately 15 mL of tryptic soy broth

281   (TSB) (BD, NJ, USA) was inoculated with a single colony of *P. aeruginosa* and

282   cultured in a shaking incubator at 37 °C and 250 rpm overnight.[49] Cells were then

283   centrifuged at 4 °C and 8000 rpm for 10 min, washed and suspended with sterile PBS

284   for the following tests.

285

286   Anti-biofilm experiments were carried out using a rotating disk biofilm reactor (DK20,

287   Biosurface, Montana, USA) under medium shear conditions. Briefly, the membrane

288   coupons were taped on the rotating disk. The biofilm was firstly formed in batch

289   mode (no flow) for 24 h with 1 mL PA14 suspension (10^6 CFU/mL) and 250 mL TSB

290   solution (300 mg/L). After reaching steady-state growth, the reactor was operated for

291   an additional 24 h with a continuous flow of the TSB solution (30 mg/L, 8.5 mL/min).

292   During the whole biofilm formation, the membrane coupon surfaces were

293   continuously exposed with fluid shear from the rotation of the disk (200 rpm). At the

294   end, the membrane coupons were removed from the disk for confocal laser scanning

295   microscopy (CLSM) (LSM700, Carl Zeiss, Jena, Germany) observation and viable

296   cell enumeration. [50, 51]

297

298   In addition, the anti-biofouling tests were conducted using a cross-flow membrane

299   module. A 4 L synthetic wastewater was recirculated using a high-pressure pump

300   (Hydra-cell pump, Wanner Engineering, Minneapolis, MN) with a flow rate of 1

301   L/min and pressure of 5 bar. Following cleaning and stabilization, the biofouling

302   experiments were initiated by injecting bacterial suspension (10^7 CFU/mL) into the

303   feed tank. After anti-biofouling, the membranes were carefully removed from the

304   module for CLSM analysis.

305

306 **RESULTS AND DISCUSSION**

307 **sMicroscopic analysis and surface properties of the membranes.**

308 Figure 1 presents the proposed chemical structure of the MPD-Cu complexes.[52]

309 Briefly, MPD was self-polymerized and initiated by Cu^{2+} and $NaIO_4$ to form Cu-MPD

310 complexes, and GA was used to improve the crosslinking degree of the resulting

311 membrane.[31, 53] Specifically, Cu^{2+} could promote this self-polymerization by

312 coordinating with MPD monomers and mediating the transfer of electrons from MPD

313 to $NaIO_4$.[52] In addition, Cu^{2+} serves as the positive-charge center in the resultant

314 complexes. After MPD monomer is oxidized, it would turn into a cationic radical and

315 cleave from the coordination. The generated radical would further attack a free MPD

316 monomer to propagate the polymer chain. Simultaneously, another free MPD

317 monomer would occupy the vacancy of the left radical and start cycle of oxidation

318 and polymerization, resulting propagated polymer chain. To confirm the formation of

319 the positively charged Cu-MPD complexes, zeta potential measurements of the plain

320 PES and Cu-MPD membranes were performed. As shown in Figure S2, the PES

321 substrate was negatively charged throughout the pH range between pH 3 to 9. In

322 contrast, the Cu-MPD NF membrane exhibited increased positive-charge density in

323 the pH range from 3 to 7.4 (the isoelectric point). The positive-charge property on the

324 surface of the membrane can be potentially ascribed to the Cu-MPD complexes

325 containing cationic copper and protonated amino groups at acidic to neutral

326 conditions.

327

328
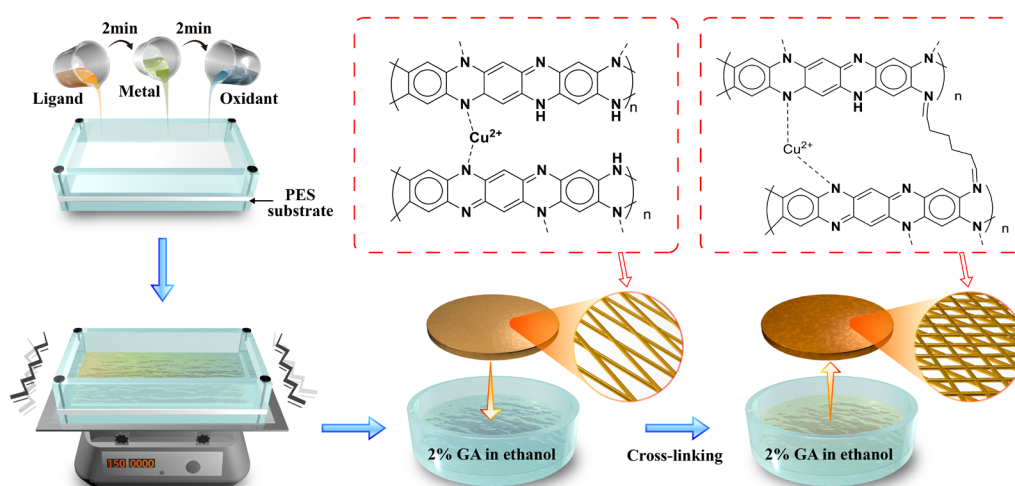
Figure 1. Membrane fabrication route and structural illustration of Cu-MPD NF membrane. MPD, $CuCl_2$ and $NaIO_4$ solution was poured onto the surface of the PES substrate, successively, followed by immersion of the surface-coated membrane into a GA/ethanol bath at 50 °C to form crosslinked Cu-MPD NF membrane.

333

To further confirm the formation of the Cu-MPD complexes, SEM and TEM techniques were applied to examine membrane surface and cross-section morphologies. As shown in Figure 2a, the pristine PES substrate had a flat surface (with root-mean-square roughness R_q of 12.2 nm in Figure 2e), with evenly distributed nanosized pores.[54] After coating the Cu-MPD complexes, the substrate pores vanished with numerous nodules prevailing on the surface of the Cu-MPD membrane (Figure 2c) with increased R_q of 22.1 nm in Figure 2f), which is in good agreement with the literature.[52] Cu-MPD membranes with different components (Table S1) and various Cu/MPD ratios were fabricated, and their morphologies and topographies were characterized through SEM (Figure S1a) and AFM (Figure S3). From there we can see that such nodules were absent when no Cu^{2+} or $NaIO_4$

345   involved in the coating process, confirming the indispensable roles of Cu^{2+} and $NaIO_4$

346   in promoting the formation of Cu-MPD complexes.[55]

348
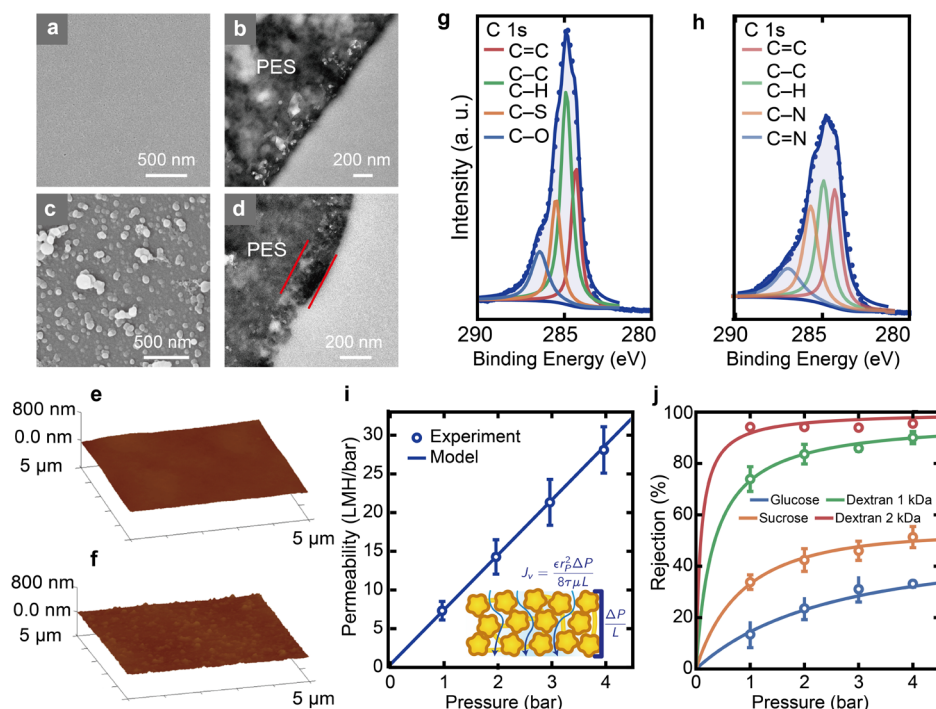
349   **Figure 2.** (a-b) SEM, (c-d) TEM, (e-f) AFM and (g-h) XPS of the prepared membrane;

350   (a, b, e, g) are for PES substrate, and (c, d, f, h) are for Cu1/2-MPD NF membrane. (i)

351   water flux against applied pressure; (j) rejection of neutral solutes under different

352   applied pressure for the Cu1/2-MPD membrane. For (i, j), dots are data obtained from

353   experimental work, and curves are model work.

354

355   TEM (Figure 2(b,d)) images present the cross-sections of the pristine PES substrate

356   and the Cu-MPD membrane. Compared to PES, the Cu-MPD membrane had a

357   thick-rejection layer of several hundred nanometers (marked between the two red

358   lines in Figure 2d). XPS was also used to confirm the formation of the Cu-MPD

359   membrane on the surface of the PES substrate (Figure 2(g,h) and Figure S4(a-c)).

360   Results in Figure 2(g,h) show the C 1s spectra of the PES substrate and the

361   Cu1/2-MPD membrane to reveal the chemical compositions of the synthesized

362   complex structure. Specifically, the deconvolution of C 1s spectrum of the PES

363   substrate (Figure 2g) showed four peaks at 284.4, 284.9, 285.3 and 286.1 eV,

364   attributed to the C=C, C-C, C-S and C-O of the backbone of the PES structure,

365   respectively.[56] In contrast, C-N and C=N were also detected in the Cu1/2-MPD

366   membrane at the bonding energy of 285.1 and 287.0 eV, respectively, in addition to

367   the peaks related with C=C and C-C of the polymerized MPD chain (Figure 2h).[53, 57]

368   N 1s spectrum was also investigated for the Cu1/2-MPD membrane to gain further

369   information of the membrane composition (Figure S4b). The peak at 399.4 eV

370   indicated the -NH, while the peak at 399.9 and 400.1 eV can be assigned to -N= and

371   -N-C, respectively. In addition, the signal of 401.1 eV indicates the presence of -N^+=,

372   which can be due to the coordination of Cu^{2+} and amino groups on the Cu-MPD

373   polymer chain.[53] The existence of Cu can also ben verified by the zeta potential

374   (Figure S4d) and isoelectric point data (Table S2), where the isoelectric point of

375   membrane Cu1/2-MPD was pH 7.4 ± 0.2 while for Cu0-MPD it was pH 5.3 ± 0.3.

376   Overall, the structural and compositional characterizations above demonstrate the

377   successful synthesis and loading of positively charged Cu-MPD onto a PES substrate.

378

379   To better understand the structure of the novel NF membrane, we use a DSPM-DE

380   model to characterize membrane porosity and pore radius. Figure 2i shows the

381   modeled and experimentally-measured water flux as a function of the applied

382   hydraulic pressure. A linear relationship is observed between water flux and hydraulic

383   pressure. The model, which is based on a Hagen-Poiseuille formulation, aligns very

384   strongly with the experiments. In Figure 2j, the rejection of each species is plotted as

385   a function of the applied hydraulic pressure. The DSPM-derived model is able to

386   capture the experimentally-observed variation of the solute rejection for all the solutes

387   tested across the range of hydraulic pressures analyzed. Solute rejection increases

388   with penetrant size in alignment with the physical intuition underlying size-based

389   selectivity. The rejection of each solute initially increases rapidly with transmembrane

390   pressure, before plateauing.[37, 39, 41] The increase in observed rejection is driven by an

391   increase in water flux, which leads to an increase in convective hindrance. As

392   transmembrane water flux continues to increase, solute rejection approachs the high

393   Péclet limit where $\text{Rej}_i \rightarrow 1 - H_{i,C}$. The fitted porosity and effective pore radius

394   obtained from the global optimization method were 0.21 and 1.25 nm, respectively.

395   Conventional nanofiltration membranes have porosities and effective pore radii that

396   range from 0.02-0.1 and 0.5-2 nm, respectively.[40, 58-62] The regressed parameters

397   suggest that the Cu-MPD membranes are significantly more porous than conventional

398   nanofiltration membranes, which aligns with observations from the SEM and TEM

399   images taken. The effective pore radius, however, is similar to current polyamide

400   membranes. The increased porosity with a comparable pore radius of synthesized

401   Cu-MPD membranes guarantees the excellent separation performance in a wide range

402   of NF-based applications beside the lithium recovery discussed below. Lastly, the

403 alignment between the model and experimental data highlights the model's predictive

404 capabilities in determining the rejection of uncharged solutes

405 coordination-complex-based membranes.

406

407 **Separation properties and lithium recovery performances of the membranes.**

408 Figure 3 presents the effect of Cu/MPD ratio on the separation performance of the

409 membranes. The actual copper loading concentration in membrane fabricated with

410 various Cu/MPD ratio was characterized with EDX (Figure S5) and ICP-OES (Table

411 S4).Without copper, the membrane exhibited relatively low rejection (22.6 ± 2.4%)

412 with low water permeance (1.3 ± 0.1 LMH/bar). With the increased Cu/MPD ratio, an

413 improved membrane water permeance and simultaneously enhanced $MgCl_2$ rejection

414 up to 90.0 ± 1.2% was observed. An optimized Cu/MPD ratio appears to be between

415 1/2 and 1, with the ratio of Cu/MPD strongly affecting the polymerization of Cu-MPD

416 complexes and therefore affecting their surface morphologies (Figure S1). We

417 speculate that the absence of copper led to the formation of incomplete and loose

418 MPD complex layer as Cu can promote the MPD self-polymerization.[52] Such a loose

419 structure could be further severely compacted at high transmembrane pressure,

420 leading to low water permeance and low $MgCl_2$ rejection. When Cu/MPD ratio

421 increased, the structure of the formed Cu-MPD complex became more rigid with

422 fewer defects, resulting in improved membrane separation performance. As the ratio

423 exceeded 1, however, synthesized Cu-MPD complex exhibited different assembly

424 pathways and decreased thickness as demonstrated by the different oligomer

425 absorption peaks in Figure S6a and QCM-D measurements in Figure S6b. This might

426 give some insight in explaining that the membrane exhibited an optimal structure with

427 Cu/MPD ratio varying 1/2 to 1. Separation performance of more membranes

428 fabricated with different components can be seen in Figure S7.

429

430 We further selected Cu1/2-MPD membrane as a benchmark to perform the lithium

431 recovery test from brine, and found its high Li^+/Mg^{2+} selectivity and high water

432 permeance (Figure 3(b,c)). Specifically, the pH of feed solution was varied from 3 to

433 9 to reveal the pH-dependent lithium recovery performance. Interestingly, unlike the

434 conventional polyamide-based NF membrane encountering the water

435 permeance-selectivity trade-off,[10] the Cu-MPD membrane demonstrated both high

436 water permeance of 16.2 ± 2.7 LMH/bar and high rejection against LiCl and $MgCl_2$ of

437 $32.3 \pm 7.6\%$ and $91.6 \pm 0.2\%$, respectively, at pH 3. The more pronounced

438 enhancement for rejecting divalent ions of $MgCl_2$ further led to a high Li^+/Mg^{2+}

439 selectivity value (8.0 ± 1.0, Figure 3b), which can be potentially due to the enhanced

440 Donnan exclusion effect, resulted from more protonated amino groups at lower pH

441 solution. At pH 9, in contrast, the membrane had systematically decreased water

442 permeance of 9.1 ± 0.7 LMH/bar and reduced rejection of LiCl and $MgCl_2$ of $21.7 \pm$

443 2.1% and $78.9 \pm 0.5\%$, respectively. Consequently, their Li^+/Mg^{2+} selectivity

444 decreased to 3.9 ± 0.1, potentially due to the neutralized membrane surface. As a

445 result, the high-performance Cu-MPD membrane at pH 3 showed relatively good

446 performance in the correlation in the upper bound diagram between membrane water

447 permeance and Li/Mg selectivity for the state-of-the-art NF membrane, including both

448 lab work and commercial membranes (Figure 3d and Table S3).[63] It is worthwhile to

449 note that different testing conditions (e.g., operating pressure, feed concentration,

450 temperature and etc.) could significantly affect membrane separation performance. In

451 order to exclude the effect of operation conditions, the correlation between water-salt

452 permselectivity A/B_{MgCl2} vs. membrane permeance A and salt-salt selectivity

453 B_{LiCl}/B_{MgCl2} vs. membrane permeance A to examine membrane intrinsic transport

454 properties were plotted in the revised Supporting Information (Figure S11).

455

456 The pH of the feed solution would greatly affect the charge density of the membrane

457 active layer by changing the protonation condition of the amino groups in the

458 Cu-MPD complex. Specifically, when pH increases, fewer amino groups are

459 protonated, leading to reduced positive charge density of membrane active layer; As a

460 result, the electrostatic repulsion between these amino group decreases, leading to a

461 tighter structure of the Cu-MPD complex. Therefore, the pore size of the membrane is

462 reduced, and vice versa. When pH decreased, more amino groups became protonated,

463 leading to higher positive charge-density. This electrostatic repulsion would result in a

464 looser structure of the Cu-MPD complex. Thus, more water could be captured and

465 enter the nano pores of the Cu-MPD complex.
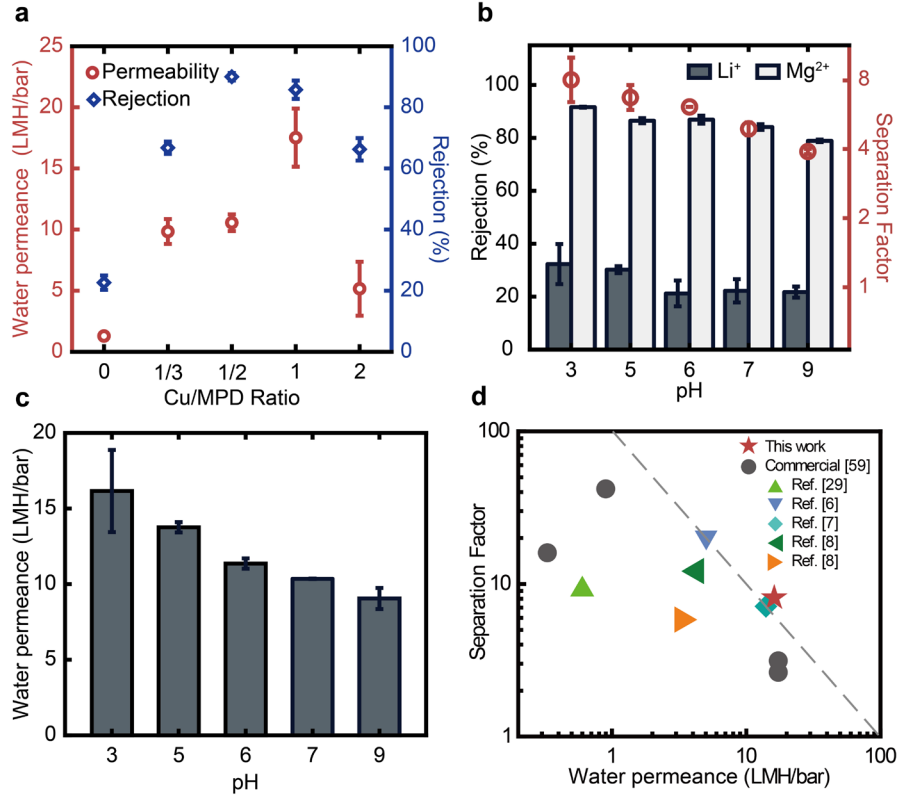
Figure 3. Separation properties and lithium recovery performances of the Cu-MPD membranes. (a) Water permeance and Mg^{2+} rejection of membrane fabricated at varied Cu/MPD ratios, (b) lithium recovery performance of Cu-MPD NF membrane as a function of pH. Membrane rejection of Li^+, Mg^{2+} and separation factor (S) of Li^+/Mg^{2+} and (c) pure water permeance in the pH range from 3-9 and (d) the performance boundary between water permeance and Li^+/Mg^{2+} separation factor, including literature results, commercial membranes and the membrane developed from this study. All filtration tests are operated at 5 bar, 1000 ppm of $MgCl_2$ was used for evaluating membrane rejection for Mg^{2+} and a synthetic brine of a concentration of 2000 ppm (Li/Mg mass ratio of 23) was used for evaluating membrane lithium recovery performance. All the presented results are based on three membrane coupons replicates.

Mechanisms of the pH-responsive properties of the membranes.

To gain a better understanding of the pH-responsive membrane properties, we further performed QCM-D analysis on the structure and mass change of the Cu-MPD membranes under different pH conditions. A significant decrease in frequency was observed when pH decreased from 9 to 3 shown in Figure 4a, implying an increased

485　mass of Cu-MPD membrane. Such an increase is caused by more-opening pore

486　structure that could accomodate more water molecules and ions. Indeed, the highest

487　Dissipation (D) value was obtained for the Cu-MPD complexes at pH 3, thanks to the

488　enhanced electrostatic repulsion for the protonated amino groups at a lower pH. The

489　looser structure further explains the enhanced water absorption (Figure 4a) as well as

490　the improved membrane water permeance (Figure 3b). On the contrary, a higher pH

491　resulted in both decreased changes in D and frequency (F) values, corresponding to a

492　more rigid layer structure and a lower water absorption, respectively. This can be

493　potentially due to the diminished charge interaction, which can be certified by the zeta

494　potential results shown in Figure S2.

495

496
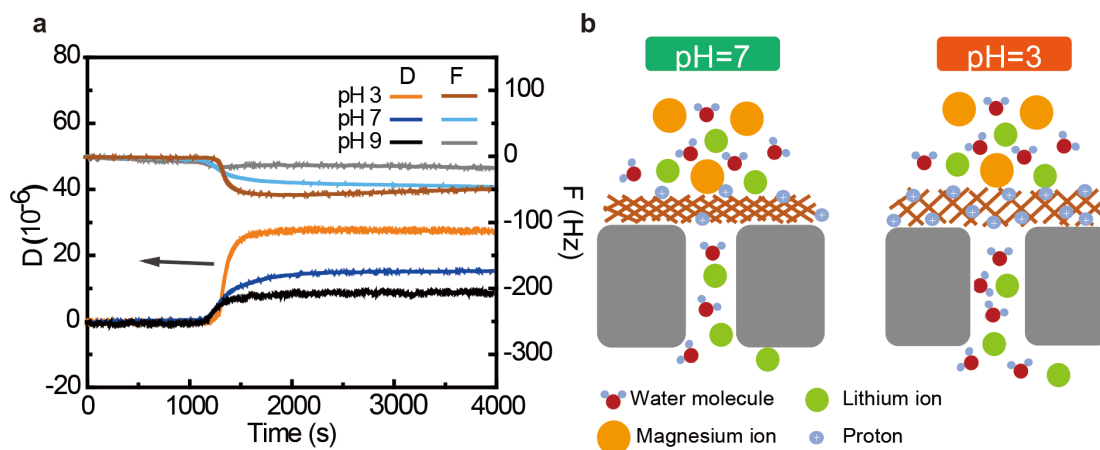
497　Figure 4. (a) QCM-D characterization of Cu-MPD NF membrane using simulated
498　brine of 2000 ppm at pH 3, 7 and 9. Cu/MPD complexes at ratio of 1/2 were coated
499　on the surface of the gold senor. To perform the charaterization, DI water was first
500　filtrated through the system for stabilizing. Subsequently, brine with different pH was
501　introduced with the real-time measured frequency and dissipation and (b) a schematic
502　illustration of a mechanism for pH-responsive membrane.

503

Antibiofouling properties of the membranes.

Conventional polyamide-based NF membranes are prone to biofouling and significantly increase its operation costs.[32] Copper is a well-known antimicrobial agent.[64, 65] In this regard, antibiofouling and antimicrobial properties of the Cu-MPD membrane were investigated. The CLSM images (Figure 5b) show reduced biofilm thickness after a 10 h filtration test for the copper-contained membrane compared to the control counterpart. Moreover, compared to the control membrane showing significant water flux loss, the Cu-MPD membrane exhibited only a slightly reduced water flux thanks to the antifouling capability as a result of the loaded copper (Figure 5a). We further performed the significance test for the two groups of data of colony forming unit (Supporting Information Figure S8), and the calculated P value is 0.03, implying a significance of the antimicrobial ability between membrane with and without copper. We also performed static antimicrobial tests using the rotating disc reactor. After 40 h rotating disc experiment, the Cu-MPD membrane and control were taken out from the reactor for CLSM imaging (Figure S9a), which showed that fewer live bacteria can be observed on the surface of Cu-MPD membrane in line with the anti-biofouling tests. In addition, more live bacteria were observed on the plate spread with bacteria suspension solutions from control, compared to that of Cu-MPD membrane (Figure S8(b,c)).
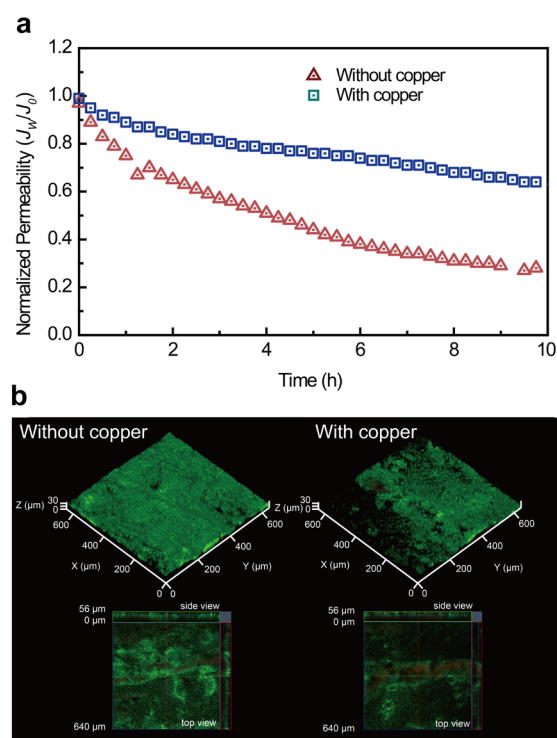
Figure 5. Anti-biofouling tests of the membranes with and without copper using a cross flow filtration system and rotating disc reactor. (a) normalized membrane water flux with and without copper, (b) CLSM image of the membrane surface with and without copper after 10 h filtration at 10 bar.

IMPLICATIONS

We developed a novel non-polyamide NF membrane with Cu^{2+} assisted MPD self-polymerization. The fabrication conditions and the effect of Cu^{2+} on membrane structure and separation performance were systematically investigated. The optimized membrane exhibited high water permeance and high Li^+/Mg^{2+} selectivity, which exceeded the upper bound of the lab-made membrane as well as commercial membranes. Furthermore, the membrane showed both increased water permeance and salt rejection at lower pH. The underlying mechanism in membrane structure and surface charge density at different pH was elucidated with the aid of QCM-D. An NF model was also developed in this work to fit water flux and rejection of uncharged

27

541 solutes to experimental data. The model was within a 2% deviation of all conducted

542 experiments. Lastly, the Cu-MPD NF membrane showed good anti-biofouling ability,

543 accounted for its Cu^{2+} loading and surface positive charge. The high porsity and

544 suitable pore radius implied by modelling and separation performance highlight the

545 great promise of Cu-MPD membranes in the fields relevant to NF applications.

546 Additionally, this method can be further extended by tuning pore size using different

547 monomers or cations for versatile applications, such as heavy metal removal and dye

548 retention.

549

550 **ASSOCIATED CONTENT**

551 The Supporting Information is available free of charge at DOI:

552 XXXXX

553

554 **AUTHOR INFORMATION**

555 **Corresponding Authors**

556 Zhongying Wang   e-mail: wangzy6@sustech.edu.cn;   tel.: +86-075588018040;

557 Zhe Yang   e-mail: zheyang@connect.hku.hk;   tel.: +852-2857 8470;

558 John H. Lienhard   e-mail: lienhard@mit.edu.;   tel.: +1-617-253-3790

559

560 **Authors**

561 **Li Wang:** 0000-0001-9829-4729

562 **Danyal Rehman:** 0000-0001-9457-191X

563 **Peng-Fei Sun:** 0000-0002-3942-9766

564 **Akshay Deshmukh:** 0000-0002-3693-1902

565 **Liyuan Zhang:** 0000-0002-7585-5607

566 **Qi Han:** 0000-0003-3493-0655

567 **Zhe Yang:** 0000-0003-0753-3902

568 **Zhongying Wang:** 0000-0002-7869-6859

569 **Hee-Deung Park:** 0000-0002-5769-335X

570 **John H. Lienhard:** 0000-0002-2901-0638

571 **Chuyang Y. Tang:** 0000-0002-7932-6462

572

573 **Notes**

574 The authors declare no competing financial interest.

575

583

References:

1. Goriparti, S.; Miele, E.; De Angelis, F.; Di Fabrizio, E.; Proietti Zaccaria, R.; Capiglia, C., Review on Recent Progress of Nanostructured Anode Materials for Li-Ion Batteries. *J. Power Sources* **2014,** *257*, 421-443.

2. Swain, B., Recovery and Recycling of Lithium: A Review. *Sep. Purif. Technol.* **2017,** *172*, 388-403.

3. Li, X.; Mo, Y.; Qing, W.; Shao, S.; Tang, C. Y.; Li, J., Membrane-Based Technologies for Lithium Recovery from Water Lithium Resources: A Review. *J. Membr. Sci.* **2019,** *591*, 117317

4. Zhao, X.; Yang, H.; Wang, Y.; Sha, Z., Review on the Electrochemical Extraction of Lithium from Seawater/brine. *J. Electroanal. Chem.* **2019,** *850*, 1572-6657.

5. Li, X.; Zhang, C.; Zhang, S.; Li, J.; He, B.; Cui, Z., Preparation and Characterization of Positively Charged Polyamide Composite Nanofiltration Hollow Fiber Membrane for Lithium and Magnesium Separation. *Desalination* **2015,** *369*, 26-36.

6. Xu, P.; Wang, W.; Qian, X.; Wang, H.; Guo, C.; Li, N.; Xu, Z.; Teng, K.; Wang, Z., Positive Charged PEI-TMC Composite Nanofiltration Membrane for Separation of Li$^+$ and Mg^{2+} from Brine with High Mg^{2+}/Li$^+$ Ratio. *Desalination* **2019,** *449*, 57-68.

7. Zhang, H.-Z.; Xu, Z.-L.; Ding, H.; Tang, Y.-J., Positively Charged Capillary Nanofiltration Membrane with High Rejection for Mg^{2+} and Ca^{2+} and Good Separation for Mg^{2+} and Li$^+$. *Desalination* **2017,** *420*, 158-166.

8. Guo, C. S.; Li, N.; Qian, X. M.; Shi, J.; Jing, M. L.; Teng, K. Y.; Xu, Z. W., Ultra-Thin Double Janus Nanofiltration Membrane for Separation of Li$^+$ and Mg^{2+}: "Drag" Effect from Carboxyl-containing Negative Interlayer. *Sep. Purif. Technol.* **2020,** *230*, 115567.

9. Quist-Jensen, C. A.; Ali, A.; Drioli, E.; Macedonio, F., Perspectives on Mining from Sea and Other Alternative Strategies for Minerals and Water Recovery-the Development of Novel Membrane Operations. *J. Taiwan Inst. Chem. Eng.* **2019,** *94*, 129-134.

10. Yang, Z.; Guo, H.; Tang, C. Y., The Upper Bound of Thin-Film Composite (TFC) Polyamide Membranes for Desalination. *J. Membr. Sci.* **2019,** *590*, 117297.

11. Zhang, Y.; Wang, L.; Sun, W.; Hu, Y.; Tang, H., Membrane Technologies for Li$^+$/Mg^{2+} Separation from Salt-Lake Brines and Seawater: A Comprehensive Review. *J. Ind. Eng. Chem.* **2020,** *81*, 7-23.

12. Ahdab, Y. D.; Rehman, D.; Lienhard, J. H., Brackish Water Desalination for Greenhouses: Improving Groundwater Quality for Irrigation Using Monovalent Selective Electrodialysis Reversal. *J. Membr. Sci.* **2020,** *610*, 118072.

13. Wen, X.; Ma, P.; Zhu, C.; He, Q.; Deng, X., Preliminary Study on Recovering Lithium Chloride from Lithium-Containing Waters by Nanofiltration. *Sep. Purif. Technol.* **2006,** *49*, (3), 230-236.

14. Ahdab, Y. D.; Rehman, D.; Schücking, G.; Barbosa, M.; Lienhard, J. H., Treating Irrigation Water Using High-Performance Membranes for Monovalent Selective

626 Electrodialysis. *ACS ES&T Water* **2020,** *1*, 117-124.

627 15. Guo, H.; Peng, L. E.; Yao, Z.; Yang, Z.; Ma, X.; Tang, C. Y., Non-Polyamide

628 Based Nanofiltration Membranes Using Green Metal-Organic Coordination

629 Complexes: Implications for the Removal of Trace Organic Contaminants. *Environ.*

630 *Sci. Technol.* **2019,** *53*, (5), 2688-2694.

631 16. Yang, Z.; Ma, X.-H.; Tang, C. Y., Recent Development of Novel Membranes for

632 Desalination. *Desalination* **2018,** *434*, 37-59.

633 17. Yang, Z.; Sun, P.-F.; Li, X.; Gan, B.; Wang, L.; Song, X.; Park, H.-D.; Tang, C. Y.,

634 A Critical Review on Thin-Film Nanocomposite Membranes with Interlayered

635 Structure: Mechanisms, Recent Developments, and Environmental Applications.

636 *Environ. Sci. Technol.* **2020,** *54*, (24), 15563-15583.

637 18. Somrani, A.; Hamzaoui, A. H.; Pontie, M., Study on Lithium Separation from

638 Salt Lake Brines by Nanofiltration (NF) and Low Pressure Reverse Osmosis (LPRO).

639 *Desalination* **2013,** *317*, 184-192.

640 19. Epsztein, R.; DuChanois, R. M.; Ritt, C. L.; Noy, A.; Elimelech, M., Towards

641 Single-Species Selectivity of Membranes with Subnanometre Pores. *Nature Nanotech.*

642 **2020,** *15*, (6), 426-436.

643 20. Sarkar, P.; Modak, S.; Karan, S., Ultraselective and Highly Permeable Polyamide

644 Nanofilms for Ionic and Molecular Nanofiltration. *Advanced Functional Materials*

645 **2021,** *31*, (3), 2007054.

646 21. Robeson, L. M., Correlation of Separation Factor versus Permeability for

647 Polymeric Membranes. *J. Membr. Sci.* **1991,** *62*, (2), 165-185.

648 22. Robeson, L. M., The Upper Bound Revisited. *J. Membr. Sci.* **2008,** *320*, (1-2),

649 390-400.

650 23. Geise, G. M.; Park, H. B.; Sagle, A. C.; Freeman, B. D.; McGrath, J. E., Water

651 Permeability and Water/Salt Selectivity Trade-Off in Polymers for Desalination. *J.*

652 *Membr. Sci.* **2011,** *369*, (1-2), 130-138.

653 24. Geise, G. M.; Paul, D. R.; Freeman, B. D., Fundamental Water and Salt Transport

654 Properties of Polymeric Materials. *Prog. Polym. Sci.* **2014,** *39*, (1), 1-42.

655 25. Werber, J. R.; Deshmukh, A.; Elimelech, M., The Critical Need for Increased

656 Selectivity, Not Increased Water Permeability, for Desalination Membranes. *Environ.*

657 *Sci. Technol. Lett.* **2016,** *3*, (4), 112-120.

658 26. Roy, Y.; Lienhard, J. H., A Framework to Analyze Sulfate versus Chloride

659 Selectivity in Nanofiltration. *Environ. Sci.: Water Res. Technol.* **2019,** *5*, (3), 585-598.

660 27. Park, H. B.; Kamcev, J.; Robeson, L. M.; Elimelech, M.; Freeman, B. D.,

661 Maximizing the Right Stuff: The Trade-Off between Membrane Permeability and

662 Selectivity. *Science* **2017,** *356*, (6343), 1137.

663 28. Werber, J. R.; Osuji, C. O.; Elimelech, M., Materials for Next-Generation

664 Desalination and Water Purification Membranes. *Nat. Rev. Mater.* **2016,** *1*, (5), 1-15.

665 29. Meshram, P.; Pandey, B. D.; Mankhand, T. R., Extraction of Lithium from

666 Primary and Secondary Sources by Pre-treatment, Leaching and Separation: A

667 Comprehensive Review. *Hydrometallurgy* **2014,** *150*, 192-208.

30. Lv, Y.; Du, Y.; Qiu, W. Z.; Xu, Z. K., Nanocomposite Membranes via the Codeposition of Polydopamine/Polyethylenimine with Silica Nanoparticles for Enhanced Mechanical Strength and High Water Permeability. *ACS Appl. Mater. Interfaces* **2017**, *9*, (3), 2966-2972.

31. Lv, Y.; Yang, H.-C.; Liang, H.-Q.; Wan, L.-S.; Xu, Z.-K., Nanofiltration Membranes via Co-deposition of Polydopamine/Polyethylenimine Followed by Cross-linking. *J. Membr. Sci.* **2015**, *476*, 50-58.

32. Yang, Z.; Wu, Y.; Wang, J.; Cao, B.; Tang, C. Y., In Situ Reduction of Silver by Polydopamine: A Novel Antimicrobial Modification of A Thin-Film Composite Polyamide Membrane. *Environ. Sci. Technol.* **2016**, *50*, (17), 9543-50.

33. Guo, H.; Yao, Z.; Yang, Z.; Ma, X.; Wang, J.; Tang, C. Y., A One-Step Rapid Assembly of Thin Film Coating using Green Coordination Complexes for Enhanced Removal of Trace Organic Contaminants by Membranes. *Environ. Sci. Technol.* **2017**, *51*, (21), 12638-12643.

34. Li, W.; Shi, C.; Zhou, A.; He, X.; Sun, Y.; Zhang, J., A Positively Charged Composite Nanofiltration Membrane Modified by EDTA for $LiCl/MgCl_2$ Separation. *Sep. Purif. Technol.* **2017**, *186*, 233-242.

35. Roy, Y.; Lienhard, J. H., Factors Contributing to the Change in Permeate Quality upon Temperature Variation in Nanofiltration. *Desalination* **2019**, *455*, 58-70.

36. Roy, Y.; Warsinger, D. M.; Lienhard, J. H., Effect of Temperature on Ion Transport in Nanofiltration Membranes: Diffusion, Convection and Electromigration. *Desalination* **2017**, *420*, 241-257.

37. Labban, O.; Liu, C.; Chong, T. H.; Lienhard, J. H., Relating Transport Modeling to Nanofiltration Membrane Fabrication: Navigating the Permeability-Selectivity Trade-Off in Desalination Pretreatment. *J. Membr. Sci.* **2018**, *554*, 26-38.

38. Roy, Y.; Sharqawy, M. H.; Lienhard, J. H., Modeling of Flat-Sheet and Spiral-Wound Nanofiltration Configurations and its Application in Seawater Nanofiltration. *J. Membr. Sci.* **2015**, *493*, 360-372.

39. Labban, O.; Liu, C.; Chong, T. H.; Lienhard, J. H., Fundamentals of Low-Pressure Nanofiltration: Membrane Characterization, Modeling, and Understanding the Multi-Ionic Interactions in Water Softening. *J. Membr. Sci.* **2017**, *521*, 18-32.

40. Ahmad, A.; Ooi, B.; Mohammad, A. W.; Choudhury, J., Composite Nanofiltration Polyamide Membrane: A Study on the Diamine Ratio and Its Performance Evaluation. *Ind. Eng. Chem. Res.* **2004**, *43*, (25), 8074-8082.

41. Geraldes, V.; Alves, A. M. B., Computer Program for Simulation of Mass Transport in Nanofiltration Membranes. *J. Membr. Sci.* **2008**, *321*, (2), 172-182.

42. Bowen, W. R.; Welfoot, J. S., Modelling the Performance of Membrane Nanofiltration-Critical Assessment and Model Development. *Chem. Eng. Sci.* **2002**, *57*, (7), 1121-1137.

43. Dechadilok, P.; Deen, W. M., Hindrance Factors for Diffusion and Convection in Pores. *Ind. Eng. Chem. Res.* **2006**, *45*, (21), 6953-6959.

710 44. Deen, W. M., Hindered Transport of Large Molecules in Liquid-Filled Pores.
711 *AIChE J.* **1987,** *33*, (9), 1409-1425.

712 45. Richards, L. A.; Richards, B. S.; Corry, B.; Schäfer, A. I., Experimental Energy
713 Barriers to Anions Transporting through Nanofiltration Membranes. *Environ. Sci.*
714 *Technol.* **2013,** *47*, (4), 1968-1976.

715 46. Sigurdardottir, S. B.; DuChanois, R. M.; Epsztein, R.; Pinelo, M.; Elimelech, M.,
716 Energy Barriers to Anion Transport in Nanofiltration Membranes: Role of Intra-Pore
717 Diffusion. *J. Membr. Sci.* **2020,** *603*, 117921.

718 47. Tunuguntla, R. H.; Henley, R. Y.; Yao, Y.-C.; Pham, T. A.; Wanunu, M.; Noy, A.,
719 Enhanced Water Permeability and Tunable Ion Selectivity in Subnanometer Carbon
720 Nanotube Porins. *Science* **2017,** *357*, (6353), 792-796.

721 48. Zhou, X.; Wang, Z.; Epsztein, R.; Zhan, C.; Li, W.; Fortner, J. D.; Pham, T. A.;
722 Kim, J.-H.; Elimelech, M., Intrapore Energy Barriers Govern Ion Transport and
723 Selectivity of Desalination Membranes. *Sci. Adv.* **2020,** *6*, (48), eabd9045.

724 49. Sun, P.-F.; Kim, T.-S.; Kim, H.-S.; Ham, S.-Y.; Jang, Y.; Park, Y.-G.; Tang, C. Y.;
725 Park, H.-D., Improved Anti-biofouling Performance of Pressure Retarded Osmosis
726 (PRO) by Dosing with Chlorhexidine Gluconate. *Desalination* **2020,** *481*, 114376.

727 50. Ham, S.-Y.; Kim, H.-S.; Jang, Y.; Sun, P.-F.; Park, J.-H.; Lee, J. S.; Byun, Y.; Park,
728 H.-D., Control of Membrane Biofouling by 6-Gingerol Analogs: Quorum Sensing
729 Inhibition. *Fuel* **2019,** *250*, 79-87.

730 51. Kim, H.-S.; Ham, S.-Y.; Jang, Y.; Sun, P.-F.; Park, J.-H.; Hoon Lee, J.; Park,
731 H.-D., Linoleic Acid, A Plant Fatty Acid, Controls Membrane Biofouling via
732 Inhibition of Biofilm Formation. *Fuel* **2019,** *253*, 754-761.

733 52. Zhang, L.; Wang, H.; Yu, W.; Su, Z.; Chai, L.; Li, J.; Shi, Y., Facile and
734 Large-Scale Synthesis of Functional Poly(m-Phenylenediamine) Nanoparticles by
735 Cu^{2+}-assisted Method with Superior Ability for Dye Adsorption. *J. Mater. Chem.* **2012,**
736 *22*, (35), 18244.

737 53. Chai, L.; Wang, T.; Zhang, L.; Wang, H.; Yang, W.; Dai, S.; Meng, Y.; Li, X., A
738 Cu–m-Phenylenediamine Complex Induced Route to Fabricate
739 Poly(m-Phenylenediamine)/Reduced Graphene Oxide Hydrogel and Its Adsorption
740 Application. *Carbon* **2015,** *81*, 748-757.

741 54. Wang, L.; Song, X.; Wang, T.; Wang, S.; Wang, Z.; Gao, C., Fabrication and
742 Characterization of Polyethersulfone/Carbon Nanotubes (PES/CNTs) Based Mixed
743 Matrix Membranes (MMMs) for Nanofiltration Application. *Appl. Surf. Sci.* **2015,**
744 *330*, 118-125.

745 55. Yu, W.; Zhang, L.; Meng, Y.; Dai, S.; Su, Z.; Chai, L.; Wang, H., High
746 Conversion Synthesis of Functional Poly(m-Phenylenediamine) Nanoparticles by
747 Cu-OH-assisted Method and Its Superior Ability toward Ag^+ Adsorption. *Synth. Met.*
748 **2013,** *176*, 78-85.

749 56. Ma, L.; Qin, H.; Cheng, C.; Xia, Y.; He, C.; Nie, C.; Wang, L.; Zhao, C.,
750 Mussel-inspired Self-coating at Macro-interface with Improved Biocompatibility and
751 Bioactivity via Dopamine Grafted Heparin-like Polymers and Heparin. *J. Mater.*

Chem. B **2014,** *2*, (4), 363-375.

57. Zhang, X.; Jia, C.; Xue, Y.; Yang, P., Fabrication of RGO/g-C$_3$N$_4$ Composites via Electrostatic Assembly towards Charge Separation Control. *RSC Adv.* **2017,** *7*, (69), 43888-43893.

58. Bowen, W. R.; Mukhtar, H., Characterisation and Prediction of Separation Performance of Nanofiltration Membranes. *J. Membr. Sci.* **1996,** *112*, (2), 263-274.

59. Košutić, K.; Dolar, D.; Kunst, B., On Experimental Parameters Characterizing the Reverse Osmosis and Nanofiltration Membranes' Active Layer. *J. Membr. Sci.* **2006,** *282*, (1-2), 109-114.

60. Wadekar, S. S.; Vidic, R. D., Influence of Active Layer on Separation Potentials of Nanofiltration Membranes for Inorganic Ions. *Environ. Sci. Technol.* **2017,** *51*, (10), 5658-5665.

61. Liang, Y.; Zhu, Y.; Liu, C.; Lee, K.-R.; Hung, W.-S.; Wang, Z.; Li, Y.; Elimelech, M.; Jin, J.; Lin, S., Polyamide Nanofiltration Membrane with Highly Uniform Sub-Nanometre Pores for Sub-1 Å Precision Separation. *Nat. Commun.* **2020,** *11*, (1), 1-9.

62. Van der Bruggen, B.; Vandecasteele, C., Modelling of the Retention of Uncharged Molecules with Nanofiltration. *Water Res.* **2002,** *36*, (5), 1360-1368.

63. Yang, G.; Shi, H.; Liu, W. Q.; Xing, W. H.; Xu, N. P., Investigation of Mg^{2+}/Li$^+$ Separation by Nanofiltration. *Chinese J Chem Eng* **2011,** *19*, (4), 586-591.

64. Ben-Sasson, M.; Zodrow, K. R.; Genggeng, Q.; Kang, Y.; Giannelis, E. P.; Elimelech, M., Surface Functionalization of Thin-Film Composite Membranes with Copper Nanoparticles for Antimicrobial Surface Properties. *Environ. Sci. Technol.* **2014,** *48*, (1), 384-393.

65. Kochkodan, V.; Hilal, N., A Comprehensive Review on Surface Modified Polymer Membranes for Biofouling Mitigation. *Desalination* **2015,** *356*, 187-207.

1

2 <u>Supporting Information</u>

A novel positively-charged metal-coordinated

nanofiltration membrane for lithium recovery

5 Li Wang[a,b], Danyal Rehman[c], Peng-Fei Sun[d], Akshay Deshmukh[c], Liyuan Zhang[b], Qi

6 Han[a], Zhe Yang[b*], Zhongying Wang[a*], Hee-Deung Park[d], John H. Lienhard[c*] and

7 Chuyang Y. Tang[b]

8 [a] School of Environmental Science and Engineering, Southern University of Science
9 and Technology, Shenzhen 518055, China
10 [b] Department of Civil Engineering, the University of Hong Kong, Pokfulam, Hong
11 Kong, SAR, P. R. China
12 [c] Department of Mechanical Engineering, Massachusetts Institute of Technology,
13 Cambridge MA 02139, USA
14 [d] School of Civil, Environmental and Architectural Engineering, Korea University,
15 Seoul, 02841, South Korea

16

17

18 [*] to whom correspondence should be addressed.

19 Zhongying Wang   e-mail: wangzy6@sustech.edu.cn;   tel.: +86-075588018040;

20 Zhe Yang   e-mail: zheyang@connect.hku.hk;   tel.: +852-2857 8470;

21 John H. Lienhard   e-mail: lienhard@mit.edu.;   tel.: +1-617-253-3790
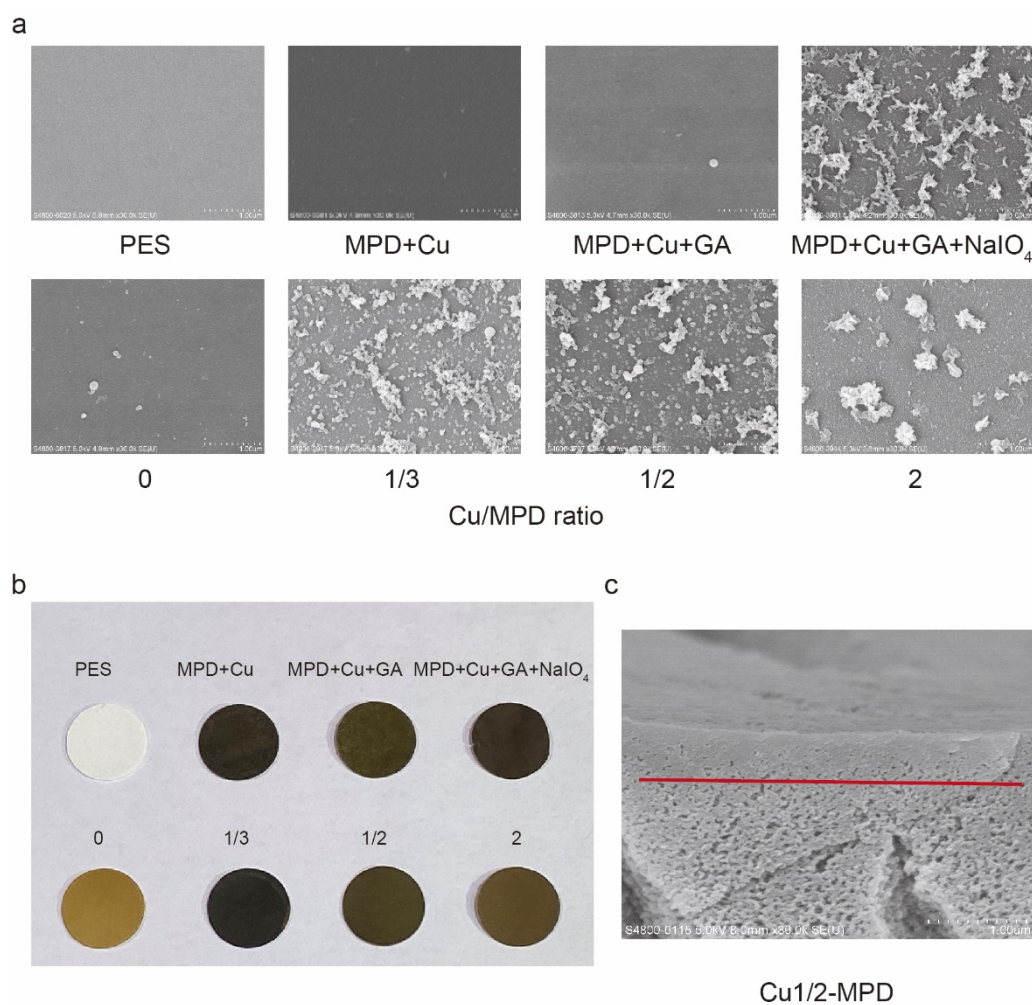
22

23

Contents

24

Figure S1. (a) SEM images of prepared membranes, (b) digital photos of prepared Cu-MPD membranes. (c) the cross-section SEM image of membrane Cu1/2-MPD.
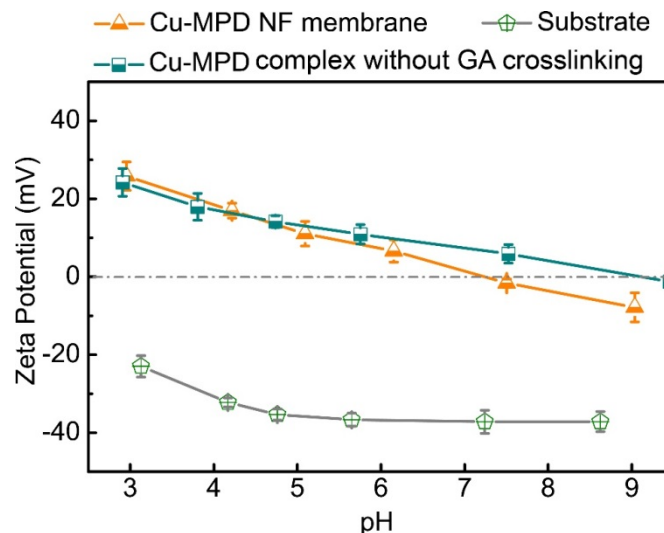
29

Figure S2. Zeta potential measurements of Cu-MPD NF membrane, Cu-MPD complex without GA crosslinking and PES substrate as a function of pH.
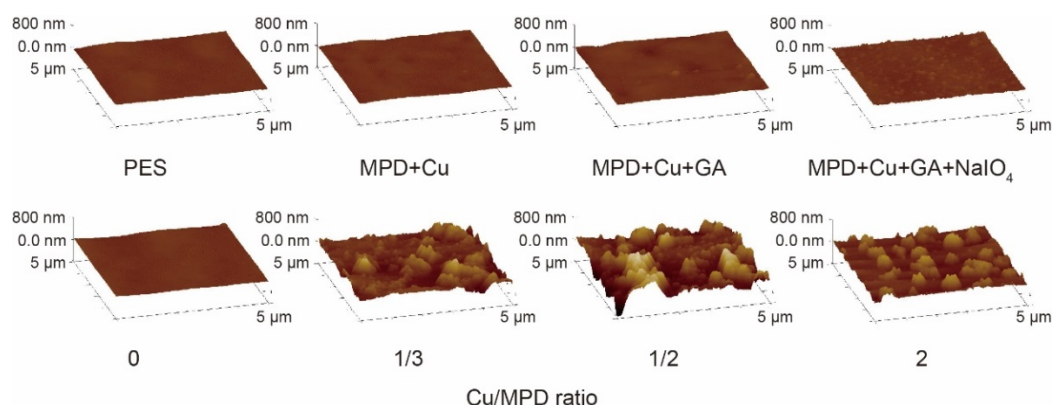
32

Figure S3. AFM images of prepared membranes with different compositions and different Cu/MPD ratios.

The amino groups in the Cu-MPD membrane contributes greatly in the positive-charge property of the membrane while the copper also plays an important role. Zeta potential of the Cu-MPD series membranes was measured at varied pH from 9 to 3. As shown in Figure S4., there was an obvious different between the trend of zeta potential for membrane Cu0-MPD and Cu1/2-MPD. We could conclude that below pH 5 the contribution of amino group dominated, while at pH higher than 5 the

43   effect of copper was significant. The two membranes also showed different

44   isoelectrical points. The isoelectrical point for Cu0-MPD was 5.3±0.3, and it was
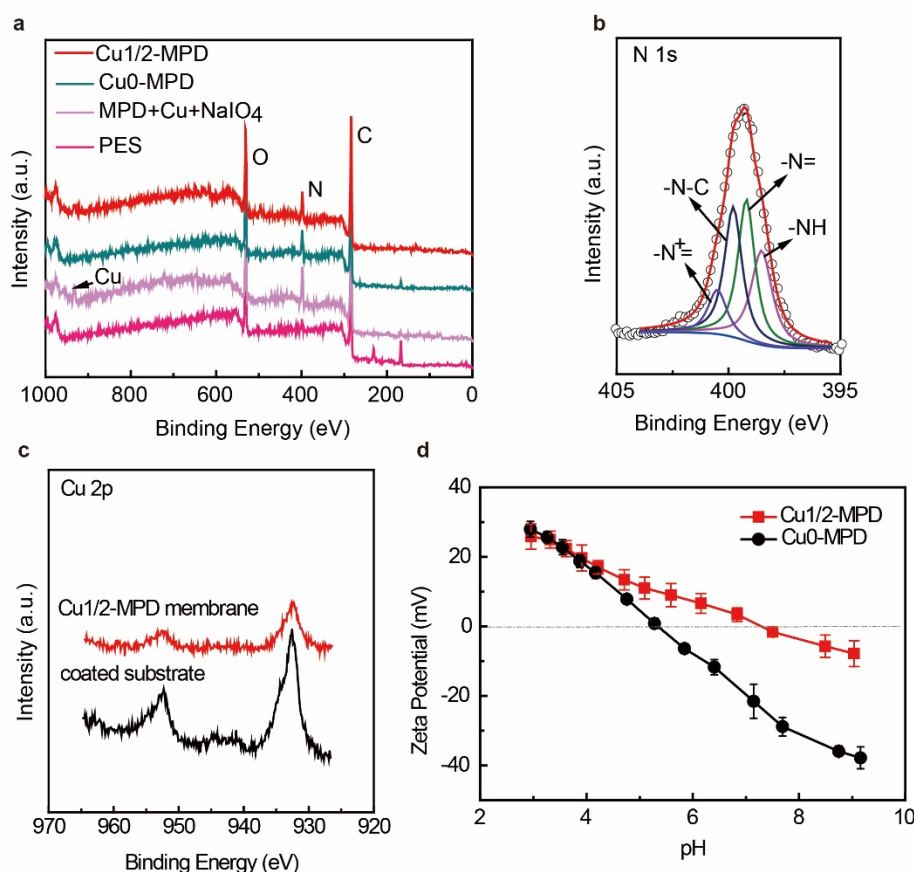
45   7.4±0.2 for Cu1/2-MPD.

46
47 **Figure S4.** (a) XPS spectra of the prepared membranes. In Cu-MPD complex coated
48 sample, XPS spectra show peaks of Cu and enlarge N signals, but the S peak
49 belonging to PES substrate disappeared due to the surface coverage with Cu-MPD
50 complex. In Cu1/2-MPD, the peak of Cu could not be clearly seen, because of the low
51 mass of Cu and the cover of GA crosslinking. (b) N 1s spectrum of the Cu1/2-MPD
52 membrane, (c) the Cu 2p XPS spectra of both Cu-MPD coated substrate and
53 Cu1/2-MPD membrane. The existence of Cu in both the NF membrane Cu1/2-MPD
54 and coated substrate are confirmed, (d) zeta potential of Cu1/2-MPD and Cu0-MPD
55 membrane. A similar surface-positive-charge density has been showed in these two
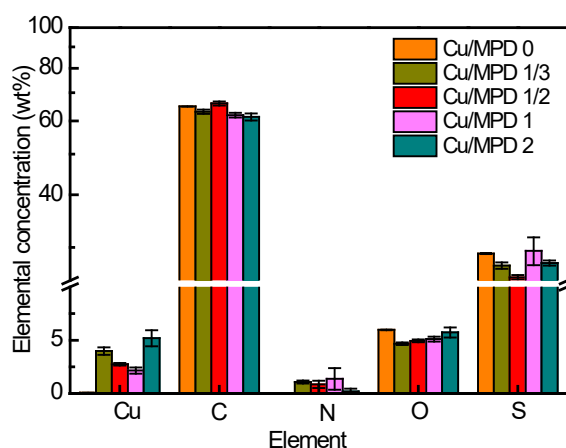56 membranes, indicating copper only plays a limit role in rejection at lower pH.

57

58 **Figure S5.** Copper loading in prepared membrane with different Cu/MPD ratios by
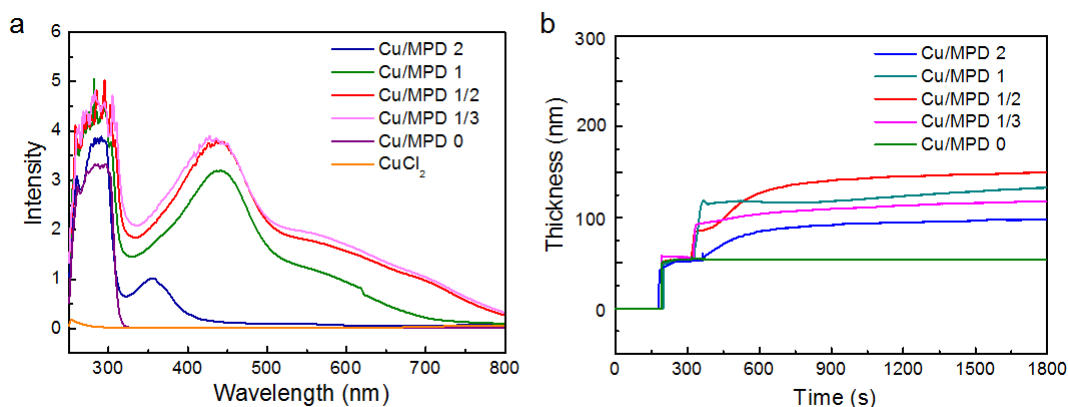59 EDX.

60

61

62 **Figure S6.** (a) UV-vis spectrum of Cu-MPD oligomers with different Cu/MPD ratios.
63 The reaction time was 30s. (b) Thickness of Cu-MPD oligomers with different
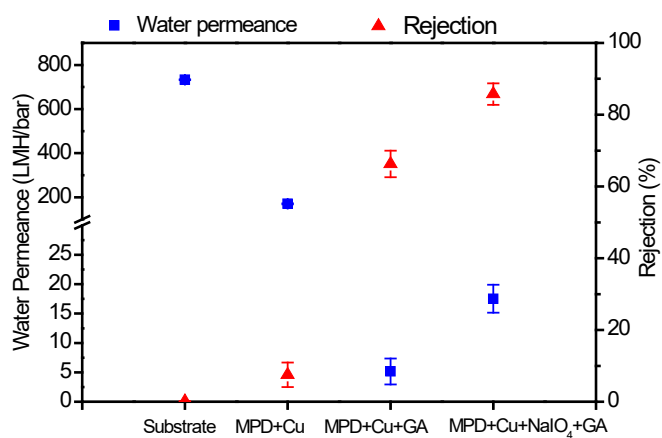64 Cu/MPD ratios.

65

66 **Figure S7.** (a) Membrane separation performance. (a) pure water permeability and
67 rejection of the PES substrate, MPD+Cu, MPD+Cu+GA, MPD+Cu+NaIO$_4$+GA (Cu

68   membrane. All filtration tests are operated at 5 bar and the feed solution concentration

69   is 1000 ppm of $MgCl_2$, which are based on three replicate membrane coupons.

70

71   **Table S1.** The recipe for fabricating the Cu-MPD membrane.

Membrane type	Cu (wt%)	MPD (wt%)	$NaIO_4$ (wt%)	GA (wt%)
Substrate	0	0	0	0
MPD+Cu	1	1	0	0
MPD+Cu+GA	1	1	0	2
MPD+Cu +NaIO₄+GA	1	1	4	2

72

73   **Table S2.** Contact angle and isoelectrical point of prepared membranes.

Membrane type (Cu/MPD ratio)	Contact angle	Isoelectrical point
Substrate	56.9±1.7	< 3
0	37.5±4.6	5.3±0.3
1/3	40.2±2.5	7.3±0.2
1/2	54.1±4.0	7.4±0.2
1	16.2±2.0	7.0±0.2
2	23.9±1.3	5.2±0.3

74

75   **Table S3.** Comparison of this work to the literature.

Surface-charge	Membrane type	Feed concent-ration	Mg/Li mass ratio	pH	SF	Permeability	Li rejection	Pressure (pre-pressure time)	Reference
		ppm	ppm/ppm			LHM/bar	%	bar (h)	
Positive	Cu-MPD	2000	23.5	3	8.0	16.16	32.3	5(2)	This work
				5	6.7	13.76	30.2		
				6	6.1	11.36	21.2		
				7	4.9	10.36	22.2		
				9	3.9	9.05	21.7		
Positive	BPEI-TMC, coated with EDTA		24	5.5	9.2	0.6	~35*	10(2)	[1]
Positive	PEI-TMC	2000	20	6.5	20	5.02	19	8(0.5)	[2]

Positive	PEI/MWCNT-TMC	2000	21.4	6.5	7.13	14.03	15	4(0.5)	3
Positive	DAPP-TMC	2000	20		2.6		-40.7*	3(0.5)	4
Negative	Janus NF membrane	2000	30		12.15	4.17	11.6	8(0.5)	5
			60		5.84	3.4	21.8	8(0.5)	
Negative	DK NF membrane (polyamide)		35.4	4	16	0.33		15(0.08)	6
Negative	NF 90	2000	20		2.1		15	3(0.5)	4
Negative	DL-2540		40		2.86		-10*		
Negative	Desal DK (GE Osmonics)	4940	18		3.13	17.36	-60*	16	
		3680	22		2.63	17.36	-30*	8	
		2500	24		2.63	27.78	-25*	10	7
Negative	DK-1812 model	6000	40		42	0.9	-170	8	

Table S4. Copper loading concentration.

Membrane type (Cu/MPD ratio)	Cu loading concentration $\mu g/cm^2$
0	ND
1/3	18.4±0.8
1/2	9.9±1.2
1	4.4±0.3
2	15.3±2.0

Membrane coupon with different components was immersed into 2% HNO_3 and shaken for 3 days, and then the Cu leaching concentration was measured by ICP-OES.

We also carried out the long-term running filtration to investigate the stability of the membrane. The testing result is presented in Figure S12. The Cu1/2-MPD membrane showed a maintained rejection in 72 h filtration, indicating its stability in long-term running application.
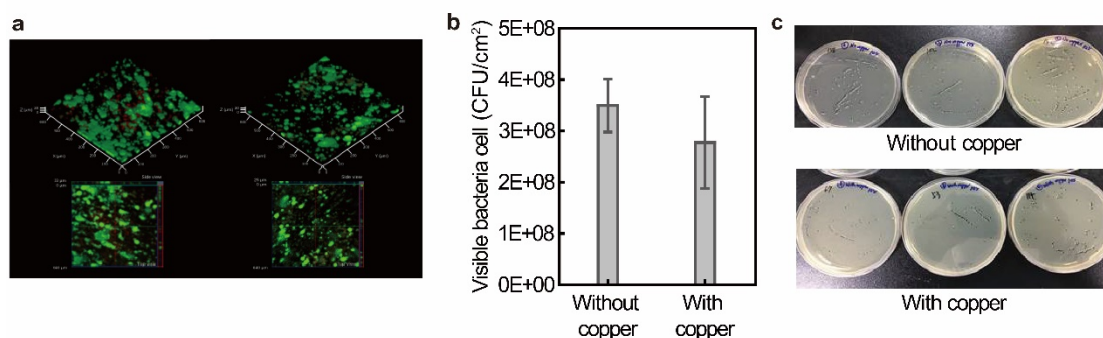
Figure S8. (a) the CLSM of membrane surface after the rotating disc filtration experiment, (b) bacteria cell number on the plates spread using the rinsing water from the membrane surface after rotating disc filtration with a P value of 0.03 and (c) digital photos of the spread plates in (b).
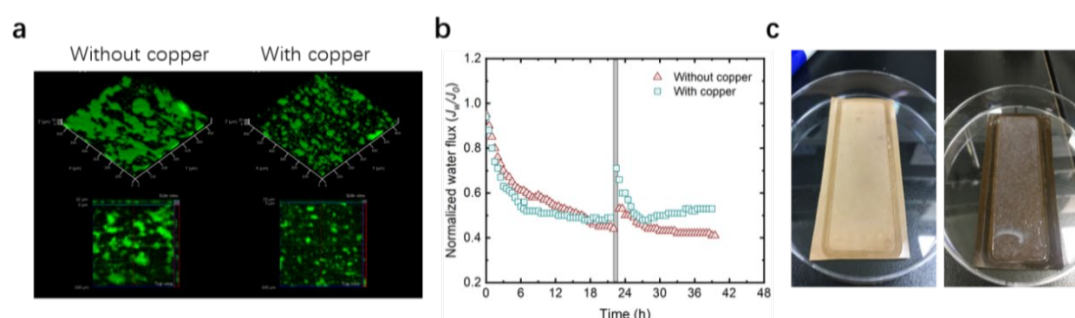

Figure S9. (a) the CLSM image of membrane surface with no copper and with Cu/MPD ratio of 1/2 after 40 h filtration at 5 bar; (b) normalized permeability of membrane with no copper and with Cu/MPD ratio of 1/2 in 40 h filtration at 5 bar; (c) the photos of membrane with no copper and with Cu/MPD ratio of 1/2 after 40 h filtration at 5 bar.
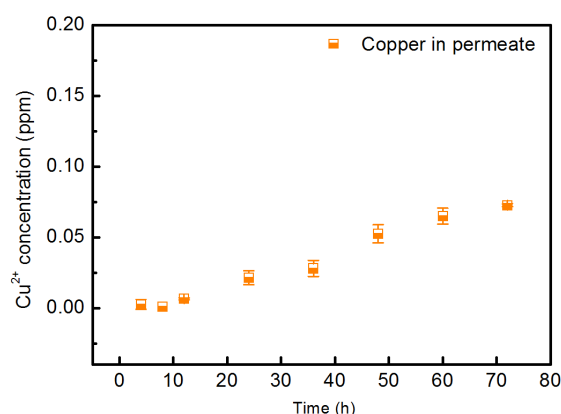

Figure S10. Copper leaching test in pure water through a dynamic cross-flow filtration for the Cu1/2-MPD membrane at pH 7 with an applied pressure of 5 bar.
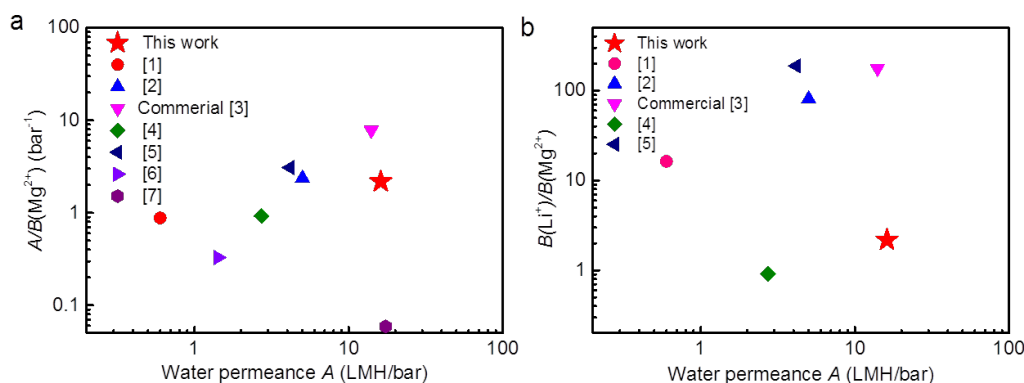
104

105 **Figure S11.** (a) Tradeoff between membrane water permeance (A) and membrane
106 water/MgCl$_2$ selectivity (A/B) and (b) Tradeoff between water permeance and
107 B_{Li+}/B_{Mg2+} ratio based on the literature survey of NF membranes and some
108 commercial NF membranes in Table S3. B value can be calculated by $J_w(1\text{-}R)/R$.

109

110   To evaluate the effect of Na$^+$ on the membrane performance, we have tested

111 membrane performance with the presence of Na$^+$. Specifically, the mass of the added

112 Na$^+$ was equal to the amount that was needed to adjust pH from 7 to 9 (we did not add

113 NaOH for brine with pH lower than 7; instead, we adjusted the pH with HCl). The

114 results show that presence of Na$^+$ didn't show any effect on the membrane

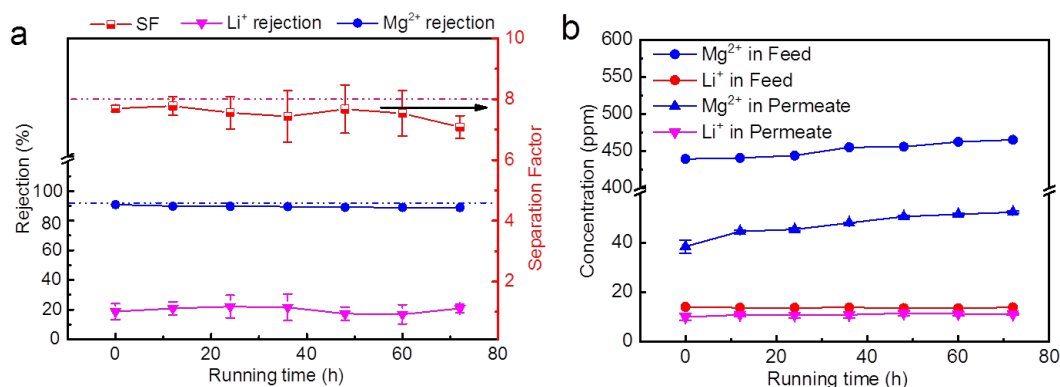115 performance in the 72 h filtration.

116

117

118

119 **Figure S12.** Membrane long-term running stability test for 72 h, pH 3, at an applied
120 pressure of 5 bar. (a) SF, Li$^+$ and Mg^{2+} rejection at the presence of Na$^+$ with
121 equivalent molar amount of NaCl to that of NaOH used adjusting from pH 7 to 9. The

122 dash line represents the corresponding control membrane without the addition of
123 NaCl and (b) the concentration of Li^+ and Mg^{2+} in permeate and feed.
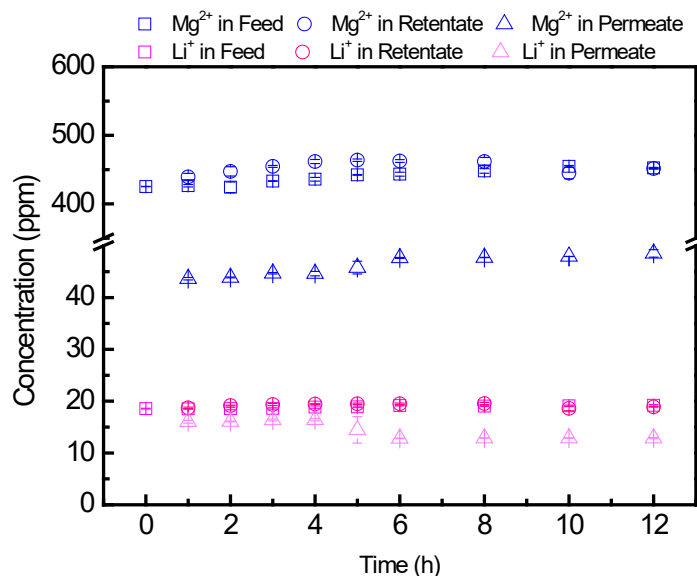124
125

126

Figure S13. Membrane separation performances tests by measuring the concentration
of Li^+ and Mg^{2+} feed, retentate and permeate solution at an applied pressure of 5 bar
for Cu1/2-MPD NF membrane at pH3.

130
131

Table S5. Average biofilm thickness and average biovolume on surface of membrane
with no copper and with Cu/MPD ratio of 1/2.

Membrane	Average biofilm thickness (µm)		Average biovolume (µm³/µm²)	
	Live cell	Dead cell	Live cell	Dead cell
No copper[1]	9.3±1.9	21.7±5.1	5.7±2.2	10.5±1.5
With copper[1]	1.9±1.5	0.5±0.4	1.3±0.9	0.2±0.1
No copper[2]	48.5±6.8	61.6±3.1	36.9±5.3	51.0±2.7
With copper[2]	36.1±8.2	43.3±14.8	21.9±5.5	29.5±15.6
No copper[3]	7.4±2.7	27.8±8.1	5.6±1.6	16.8±6.0
With copper[3]	9.8±5.1	18.3±5.7	7.4±4.1	14.1±4.9

134 Note

135 [1] membrane after 10 h filtration at 10 bar;
136 [2] membrane after 40 h filtration at 5 bar.
137 [3] membrane after rotating disc filtration.

138

139   The ICP samples have been filtrated by 0.22 µm PES filter in order not to

140 contaminate the ICP. Therefore, I and Cu, that facilitate the formation of the Cu-MPD

141 complexes, may also be filtered out within its large-sized aggregates. Considering that

142 it is beyond the current scope of this work, we decide not to over-interpret these

143 results. However, future studies could address this issue through advanced

144 characterization techniques.

145

146 **Table S6.** I and Cu concentration before and after 5h reaction. All samples have been
147 diluted for 1000 times.

Sample	I (ppm)	Cu (ppm)
0h	3.28±0.26	2.28±0.02
5h	3.06±0.03	2.44±0.03

148

149

150 **Table S7**. Performance of membrane with different recipes.

Membrane Type	Permeability (LMH/bar)	$MgCl_2$ Rejection (%)
Cu0-MPD-GA	1.9 ± 0.1	22.5 ± 2.4
Cu1/2-MPD-GA	10.6 ± 0.7	90.0 ± 1.2
Cu0-MPD-GA0	96.6 ± 6.6	6.5 ± 1.7
Cu1/2-MPD-GA0	53.3 ± 4.1	54.8 ± 4.6

151 Notes: GA0 and Cu0 mean no GA or Cu was incorporated during the polymerization
152 process.

153

154 **Table S8**. The recipe of the membranes in Table S7.

Membrane type	Cu (wt%)	MPD (wt%)	$NaIO_4$ (wt%)	GA(wt%)
Cu0-MPD-GA	0	2	4	2
Cu1/2-MPD-GA	1	2	4	2
Cu0-MPD-GA0	0	2	4	0
Cu1/2-MPD-GA0	1	2	4	0

155

156

157

158

159 **References:**

160 1. Li, W.; Shi, C.; Zhou, A.; He, X.; Sun, Y.; Zhang, J., A Positively Charged
161 Composite Nanofiltration Membrane Modified by EDTA for $LiCl/MgCl_2$ Separation.
162 *Sep. Purif. Technol.* **2017,** *186*, 233-242.
163 2. Xu, P.; Wang, W.; Qian, X.; Wang, H.; Guo, C.; Li, N.; Xu, Z.; Teng, K.; Wang,
164 Z., Positive Charged PEI-TMC Composite Nanofiltration Membrane for Separation of
165 Li^+ and Mg^{2+} from Brine with High Mg^{2+}/Li^+ Ratio. *Desalination* **2019,** *449*, 57-68.
166 3. Zhang, H.-Z.; Xu, Z.-L.; Ding, H.; Tang, Y.-J., Positively Charged Capillary
167 Nanofiltration Membrane with High Rejection for Mg^{2+} and Ca^{2+} and Good
168 Separation for Mg^{2+} and Li^+. *Desalination* **2017,** *420*, 158-166.
169 4. Li, X.; Zhang, C.; Zhang, S.; Li, J.; He, B.; Cui, Z., Preparation and
170 Characterization of Positively Charged Polyamide Composite Nanofiltration Hollow
171 Fiber Membrane for Lithium and Magnesium Separation. *Desalination* **2015,** *369*,
172 26-36.
173 5. Guo, C. S.; Li, N.; Qian, X. M.; Shi, J.; Jing, M. L.; Teng, K. Y.; Xu, Z. W.,
174 Ultra-Thin Double Janus Nanofiltration Membrane for Separation of Li^+ and Mg^{2+}:
175 "Drag" Effect from Carboxyl-containing Negative Interlayer. *Sep. Purif. Technol.*
176 **2020,** *230*, 115567.
177 6. Li, Y.; Zhao, Y.; Wang, H.; Wang, M., The Application of Nanofiltration
178 Membrane for Recovering Lithium from Salt Lake Brine. *Desalination* **2019,** *468*.
179 7. Yang, G.; Shi, H.; Liu, W. Q.; Xing, W. H.; Xu, N. P., Investigation of Mg^{2+}/Li^+
180 Separation by Nanofiltration. *Chinese J Chem Eng* **2011,** *19*, (4), 586-591.

181